Received: 10 August 2023 | Revised: 12 September 2023 | Accepted: 22 September 2023

DOI: 10.1111/rge.12321

ORIGINAL ARTICLE

RESOURCE GEOLOGY WILEY

An integrated approach for rapid exploration of carbonatites and related mineral resources

Asad Khan[1] | **Muhammad Ali**[2] | **Saad Khan**[2] | **Zaheen Ullah**[3] | **Shah Faisal**[2] | **Laeiq Ahmad**[4]

[1]Department of Earth Sciences, FATA University, FR Kohat, Pakistan

[2]National Centre of Excellence in Geology, University of Peshawar, Peshawar, Pakistan

[3]Department of Geology, University of Baltistan, Skardu, Pakistan

[4]Department of Geology, University of Swabi, Swabi, Pakistan

Correspondence
Asad Khan, Department of Earth Sciences, FATA University, FR Kohat 26100, KP, Pakistan.
Email: asadgeo89@gmail.com

Abstract

Carbonatites are proven significant repositories of several critical and strategic elements such as rare earth elements, niobium, thorium, and uranium. Owing to their economic significance, mapping of carbonatites and associated mineral deposits has occupied prominent place in mineral resource exploration programs. In this study an integrated approach was developed to map carbonatite and related mineral deposits in the Loe-Shilman, Northwest Himalaya of Pakistan, using remotely sensed advance space-borne thermal emission and reflection radiometer (ASTER) multispectral data and visible near infrared and short-wave infrared (VNIR-SWIR) spectral characteristics of minerals in these deposits. Several image enhancement techniques, including band ratio (i.e., B4/B3), principal component and minimum noise fraction transformation (PC6 and MNF5, respectively) helped in highlighting the targeted rocks. The results demonstrate the suitability of ASTER data for discriminating carbonatite related mineral deposits from other surrounding lithologies. Results obtained from these methods were validated through field observations in the area and further confirmed through petrographic and chemical analyses of collected specimens. Field data have also served as training data to perform a supervised classification, allowing further improvement of the mapping results. Moreover, the obtained results from the techniques used for exploring carbonatites and related mineral deposits were stacked together for comparison with each other, to check their sensitivities, and assess their efficiency and accuracy. Generally, all these methods successfully highlighted carbonatites and related mineral deposits; however, when used integratively they exhibit higher degree of accuracy, and has proven to be relatively rapid and cost-effective.

KEYWORDS

ASTER data, carbonatites and related minerals, mineral resources exploration, remote sensing

1 | INTRODUCTION

Carbonatites are unusual magmatic rocks and has been remained as the primary source of economic mineral deposits, including the rare earth elements, niobium, tantalum, titanium, which are vital element in the development of emerging industries and green technologies (e.g., Chakhmouradian et al., 2015; Groves &

Gwalani, 2004; Su et al., 2019 and references therein). They also host significant iron, zirconium, thorium, uranium, phosphorus and fluorine deposits that are usually related to magmatic and/or weathering processes (e.g., Ouabid et al., 2021; Toledo et al., 2004; Zaitsev et al., 2015). A number of other economic metals are also produced as by-product during metallurgical process, which include Au, Ag, Ta, and platinum group element. Consequently, worldwide many exploration programs have been brought out in recent times for carbonatites and associated deposits to develop and diversify the supply source for critical metals. The utility of remote sensing techniques to delineate and discover occurrences of carbonatite and associated mineral deposits particularly in remote areas has been approved a time- and cost-effective approaches, especially in arid regions. The Advanced Space-borne Thermal Emission and Reflection Radiometer (ASTER) data have been effectively used for exploring carbonatites and related mineral deposits (CRMD) by using several image processing techniques (e.g., Mars & Rowan, 2011; Rajendran & Nasir, 2013). ASTER data offer relatively better spatial and spectral resolutions compared to other multispectral sensors such as Sentinel -2 and Landsat, which make ASTER data more suitable for mapping carbonatite deposits. The carbonatite rocks of the Khaneishen volcanic region in Afghanistan have been delineated by the ASTER data by using band rationing and decorrelation stretch methods (e.g., Mars & Rowan, 2011). Similarly, the spectral absorption properties due to molecular reflection and absorption characteristics of carbonate minerals in the Visible and Near Infrared-Short Wave Infrared (VNIR-SWIR) region of ASTER, have been used to discriminate carbonatite deposits in Oman (e.g., Rajendran & Nasir, 2013). Similar spectral characteristics of most indicative minerals of carbonatite and associated iron oxide-apatite deposits have been implicated to band ratio, Principal Component Analysis (PCA) and Minimum Noise Fraction (MNF) algorithms for mapping carbonatite and iron oxide-apatite deposits in Gleibat Lafhouda, Morocco (e.g., Malainine et al., 2022). ASTER VNIR-SWIR data have also been subjected to PCA to investigate outcrops of carbonatites in Batein Nappe of Oman (e.g., Rajendran & Nasir, 2013). However, the occurrence of other lithologies in the targeted area having similar spectral characteristics usually complicate the process of remote sensing based mapping, particularly when the approach is based only on one method like gray scale image visualization through band ratio and/or RGB color composites.

The northwestern Himalayan region of Pakistan host several alkaline-carbonatite complexes with potential resources of critical metals. These complexes are mainly occurring around the northern margin of Peshawar plain and south of the Himalayan Main Mantle Thrust (Figure 1a), which include: (1) Loe-Shilman complex in the vicinity of Pakistan-Afghanistan border (e.g., Jan et al., 1981; Khan, Faisal, Larson, et al., 2021; Khan, Faisal, Ullah, et al., 2021), (2) Sillai Pattai, (3) Koga, and (4) Jambil carbonatites further eastward (e.g., Hong et al., 2021; Khan et al., 2023). Preliminary investigation in the Loe-Shilman carbonatite complex has revealed promising niobium and rare earth elements mineralization (e.g., Khan, Faisal, Ullah, et al., 2021). Despite of having potential of critical mineral deposits, the geology of the Loe-Shilman carbonatite complex and its extension in the area remains poorly understood because of remoteness, inaccessibility and restricted mobility in the area. Therefore, geological mapping approaches based on the interpretation of remote sensing data can contribute in improving our understanding of this area's geology. This study highlights the potential of ASTER data to identify and map carbonatites and related mineral deposits. In this regard, ASTER data were subjected to several image enhancement techniques (band rationing, PCA, MNF and supervised classification) to highlight the extension of the carbonatite complex and associated mineral deposits. The integration of these multiple techniques was used to elude false detection of material of interest and enhance accuracy of the mapping. This integrated approach has been applied in the Loe-Shilman carbonatite complex, northwestern Himalaya of Pakistan in order to evaluate the efficiency of ASTER and of this integrated approach, using field and petrographic observations, and geochemical x-ray fluorescence analysis for validation (e.g., Khan et al., 2020; Raji et al., 2021).

2 | GEOLOGICAL SETTING OF THE STUDY AREA

Northwestern Pakistan is comprised of diverse tectonic terrains, which include the Cretaceous Kohistan Island Arc (KIA), the Euro-Asian and Indian continents. The KIA is sandwiched between the colliding Euro-Asian and Indian continents along regional thrust zones known as the Main Karakorum Thrust (MKT) and Main Mantle Thrust (MMT) to the north and south, respectively (e.g., Burg, 2011; Jagoutz et al., 2009; Khan et al., 2009; Rehman et al., 2011; Searle & Treloar, 2010). The Loe-Shilman carbonatite complex is intruded within the Proterozoic to Devonian meta-sedimentary rocks of the Indian plate in the northwestern Himalayan collisional margin and is the largest carbonatite intrusion of Pakistan (with 2.4 km × 180 m in length and width; respectively; Jan et al., 1981; Khan, Faisal, Larson, et al., 2021; Khan, Faisal, Ullah, et al., 2021).

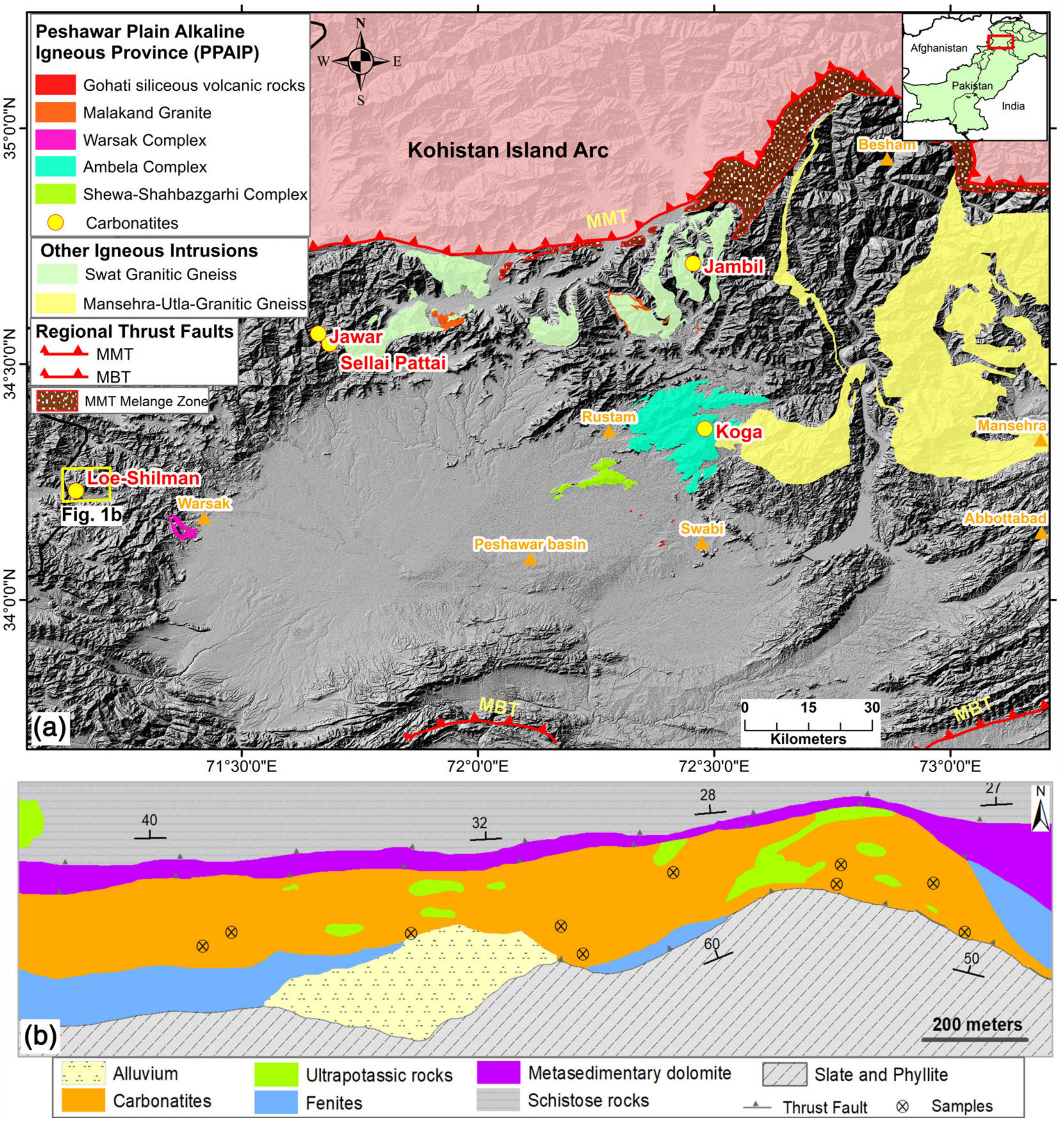

FIGURE 1 Map showing (a) carbonatites occurrences in the NW Pakistan (the geological details, adopted from DiPietro and Isachsen (2001), are overlaid on ASTER digital elevation model of the area) and (b) various lithologies of the Loe-Shilman carbonatite complex and surrounding host rocks (modified after Jan et al., 1981; Mian & Le Bas, 1988; Khan, Faisal, Larson, et al., 2021; Khan, Faisal, Ullah, et al., 2021).

The complex is a north dipping and an East–West trending tabular body of carbonatites with variable thickness and contain subordinate ultrapotassic-alkaline silicate rocks in patches (e.g., Khan, Faisal, Larson, et al., 2021; Khan, Faisal, Ullah, et al., 2021; Figure 1b). The complex is bounded by the Paleozoic (Cambrian—Devonian) meta-sedimentary rocks and minor mafic rocks (dolerites) in the north and Proterozoic slate and phyllite in the south (e.g., Jan et al., 1981; Khan, Faisal, Larson, et al., 2021; Khan, Faisal, Ullah, et al., 2021; Mian & Le Bas, 1988). The surrounding country rocks of the complex (i.e., slate, phyllite, recrystallized carbonates and quartzite, and schistose rocks) are subjected to regional metamorphism of up to biotite zone, and at placed have experienced substantial alteration as a result of fenitization (e.g., Jan et al., 1981; Mian & Le Bas, 1988). The complex submerges under the Kabul River in its west and might extend further into Afghanistan, where it has not been studied yet.

3 | DATA AND METHODS

3.1 | Acquisition and correction of data

A multispectral ASTER level 1T scene (AST_L1T) covering the Loe-Shilman area is used (Table 1), which are acquired from the Land Processing Distribution and

TABLE 1 Detail information about the ASTER scene used in this study.

Information type	Value
Granule ID	AST_L1T_00310272003061152_20150501084151_89285
Processing level ID	L1T
Acquisition date	2003-10-27
Source data product	ASTL1A 0310270611520311090528
Production date	2015-05-01
Scene center	34.0270588715735, 70.968053
Scene upper left	34.3682013343316, 70.5204766999192
Scene upper right	34.3534578345728, 71.4330867845996
Scene lower left	33.697973396652, 70.5085641417997
Scene lower right	33.6835949492043, 71.4140379559571
Solar direction	164.217254, 41.90206

TABLE 2 Characteristics of the ASTER sensor used in this study.

Subsystem	Band no.	Spectral range (mm)	Spatial resolution (m)	Signal quantization levels (bits)
VNIR	1	0.52–0.60	15	8
	2	0.63–0.69		
	3N	0.78–0.86		
	3B	0.78–0.86		
SWIR	4	1.600–1.700	30	8
	5	2.145–2.185		
	6	2.185–2.225		
	7	2.235–2.285		
	8	2.295–2.365		
	9	2.360–2.430		
TIR	10	8.125–8.475	90	12
	11	8.475–8.825		
	12	8.925–9.275		
	13	10.25–10.95		
	14	10.95–11.65		

Active Archives Center (LPD-AAC; https://LPD-AAC.usgs.gov). The ASTER_L1T data are generated from AST_L1B radiance data, which have been geometrically and terrain corrected. The downloaded scene of the study area was registered into Universal Transverse Mercator (UTM) zone 42 North as this zone cover the study area. ASTER is a multispectral sensor launched in 1999, onboard the Earth Observing System (EOS) Terra platform. Since long, ASTER data have been effectively used for exploration of various minerals and lithological mapping by several workers (e.g., Khan et al., 2020; Malainine et al., 2022; Mashkoor et al., 2022; Traore et al., 2022). ASTER sensor has relatively bettered spatial and spectral resolutions as compared to most other multispectral satellite data such as Spot -2, Sentinel -2, and Landsat images. It records reflected radiation in nine bands between 0.52 and 2.43 μm, in visible near infra-red and short-wave infra-red region of electromagnetic radiation with 15–30 m spatial resolution (e.g., Abrams, 2000; Fujisada, 1995; Yamaguchi et al., 1999). Besides, ASTER sensor measures thermal infrared wavelength in five bands between 8.125 and 11.65 μm with 90 m spatial resolution (Table 2). These ameliorated spectral and spatial characteristics makes ASTER sensor more successful for exploration and mapping of carbonatites and related mineral deposits.

The ASTER TIR data were not used because of its coarse resolution. Instead, the VNIR and SWIR ASTER bands were stacked in one file of nine bands and resized to 15 m spatial resolution. The nine banded single file was

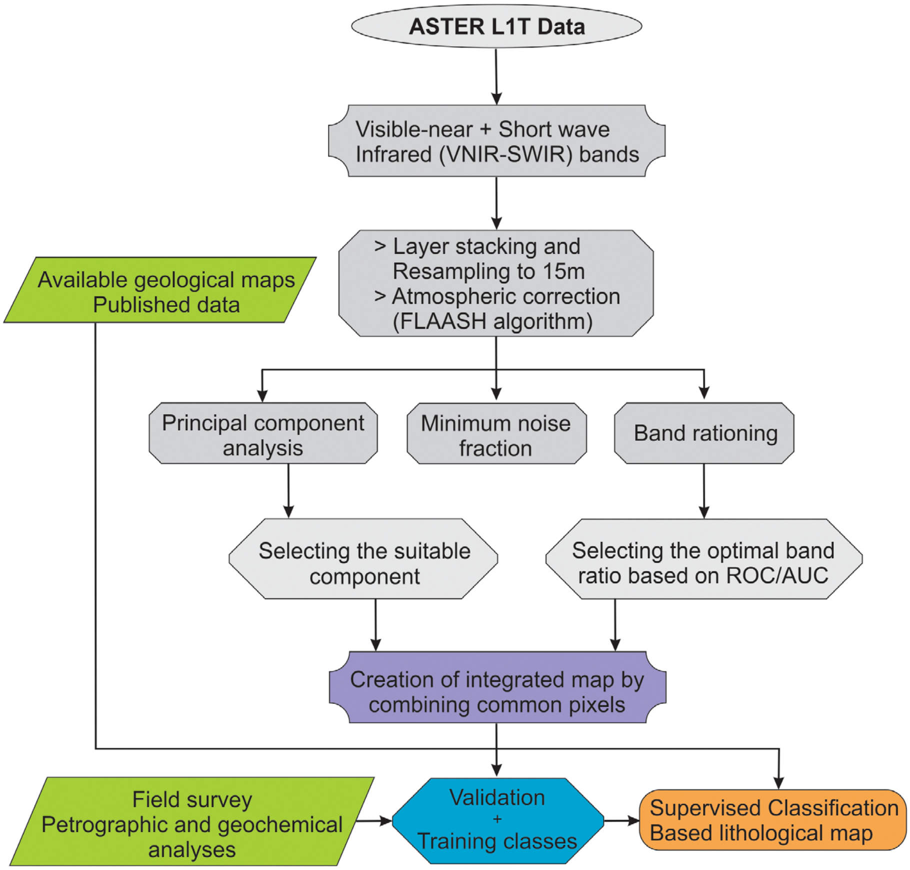

FIGURE 2 Showing data and procedures followed in this study.

then atmospherically corrected using the FLAASH (Fast Line of sight Atmospherics Analysis to Hyparcubes) module (e.g., Adler-Golden et al., 1998; Cooley et al., 2002) for converting radiance at sensor data to surface reflectance and eradicating the effects produced by water vapor and cloud cover during recording of the data. The stacked image was then subset to the study area. At the end, several procedures of image classification for enhancement of desired material were applied on the nine VNIR and SWIR bands of ASTER data, such as band ratios, PCA and MNF. Details of procedures and data used in this study are summarized in Figure 2. All the data analyses including pre-processing and image classification were carried out using ENVI (Environment for Visualizing Images) version 5.1 and then subjected to ArcGIS 10.5 for reclassification and integration of the obtained results.

3.2 | Band ratio VNIR-SWIR

Band rationing is an extensively used method for investigating and mapping various mineral deposits, ore deposits related hydrothermal alteration and weathering zones, and other rock types, for example, limestone, gypsum, peridotites and several other acidic and mafic-ultramafic igneous rocks (e.g., Amer & Kusky, 2022; Khan et al., 2020; Malainine et al., 2022; Traore et al., 2022 and references therein). It is the ratio of the digital numbers (DN) of individual pixels in different bands used and highlights the desired material in bright pixels. The selection of suitable bands to be subjected to band rationing depends on the absorption and reflection signatures of the material of interest in electromagnetic spectrum and the abundance of desired material in the scene (e.g., Clark, 1999; Pour & Hashim, 2011; Sabins, 1999).

Major composition of carbonatites is the carbonate minerals (e.g., calcite and dolomite), which have several diagnostic spectral characteristics. These minerals can be distinguished in the VNIR-SWIR region of electromagnetic radiations between 2.33 and 2.45 μm due to the spectral absorption of CO_3^{2-} anions (e.g., Clark, 1999; Mars & Rowan, 2010; Ninomiya, 2002; Rajendran & Nasir, 2014; Son et al., 2022; Traore et al., 2022). In the VNIR region of spectrum, iron-oxide/hydroxides have spectral characteristic absorption signatures around 0.455 and 0.815 μm due to the ferrous (Fe^{2+}) and ferric (Fe^{3+}) iron ions (e.g., Clark, 1999). These signatures in respective ASTER spectral bands were tested to select the most suitable band ratio for exploring CRMD. The spectral curves of the most distinctive minerals occur in carbonatites were acquired from the USGS spectral library, and were resized to ASTER band-pass (e.g., Kokaly et al., 2017; Pour & Hashim, 2011).

A database of occurrences of carbonatites and related mineral deposits was established during field work in the study area and from previously known locations (e.g., Khan, Faisal, Larson, et al., 2021; Khan, Faisal, Ullah, et al., 2021). In order to assess the performance of various band ratios used for highlighting carbonatites and related mineralization, the digital numbers of each band ratio and the corresponding sample from the database were plotted in the Receiver Operating Characteristic (ROC) curves (e.g., Nykänen et al., 2015). The curves were created by plotting sensitivity (true positive rate) against 1-specificity (false positive rate) at varying thresholds. The Area Under Curve (AUC) was used as an indicator to quantify the performance of the various band ratios used.

3.3 | Principal Component Analysis (PCA)

The PCA is procedure of transforming a multivariate data set of inter-correlated variables into a data set of new uncorrelated linear combinations of variables in such a way that the first linear combination, or principal component, measures for as much of the variance in the data as possible and each subsequent component has smaller variance (e.g., Crosta et al., 2003; Khan et al., 2020; Mars & Rowan, 2011; Ninomiya et al., 2005; Pour & Hashim, 2011; Qari et al., 2008; Singh & Harrison, 1985). The PCA is a recognized method of image classification and enhancement by compressing and narrowing the data of different bands within the first few bands (e.g., Loughlin, 1991; Öztan & Süzen, 2011).

The PCA is an efficient statistical method of highlighting spectral characteristics of exposed geological material by subduing the irradiance effects that exist in all bands (e.g., Crosta et al., 2003; Loughlin, 1991; Sabins, 1999; Tobin et al., 2007). The PCA has been used successfully for lithological mapping and mineral exploration with several advantages, including narrowing the variance of an image into a single or two bands, a segregation and transformation of noise into less correlated bands and enhancing spectral variation between surface materials that may otherwise be hidden in individual bands (e.g., Crosta et al., 2003; Öztan & Süzen, 2011). The PCA was applied on ASTER VNIR-SWIR bands to delineate carbonatites and related mineralization from surrounding rocks in the study areas.

3.4 | Minimum Noise Fraction (MNF)

Like PCA, the MNF transformation is also an efficient technique for reducing initially a large data set to a smaller number of components that contain low incoherent data and most inherent spectral information (e.g., Green et al., 1988). The MNF differentiate noise in the image data and ease the computational necessities for succeeding processing (e.g., Boardman et al., 1995; Green et al., 1988; Pour & Hashim, 2011). The MNF transformation happens in two steps; first is called noise-whitening which is calculation of principal components for decorrelating and rescaling the noise in the data from noise covariance matrix. The second step is derivation of the principal components from the noise free (whitened) data. The data is then divided into two parts: one part is having large eigenvalues and the other part is having eigenvalues near unity and noise dominated images. Using data with large eigenvalues collect the noise from the data, and enhance spectral outputs (e.g., Boardman et al., 1995; Green et al., 1988; Pour & Hashim, 2011). MNF transformation can highlight the locations of spectral anomalies, which are of interest to exploration geologist. MNF was also applied on ASTER VNIR-SWIR bands and the results were compared and integrated with those of PCA and band ratios to better highlight carbonatites and related mineral deposits from surrounding rocks in the study areas.

3.5 | Methods integration and accuracy assessment

The study area was visited to assess the success of the methods applied for delineating CRMD. Common carbonatite outcrops highlighted by all of the methods were checked by collecting field observation and sampling them for petrographic and chemical analyses. The methods applied give different results, may be due to their different sensitivities to detect carbonatites and related mineral deposits. Therefore, to compare the success of the methods applied spatially, a relative accuracy assessment was carried out. For this purpose, the resultant images were reclassified in Geographic Information System (Arc GIS 10.8) to extract pixels representing CRMD in each method. The pixels that represent CRMD were assigned a value 1 while the other pixels were valued 0. Then the extracted carbonatite pixels were combined and an integrated map with three different classes was generated.

3.6 | Supervised classification

The obtained results and field date were used as training classes to perform a supervised classification using the maximum likelihood (ML) algorithm. The ML algorithm is one of the widely used techniques for remotely sensed

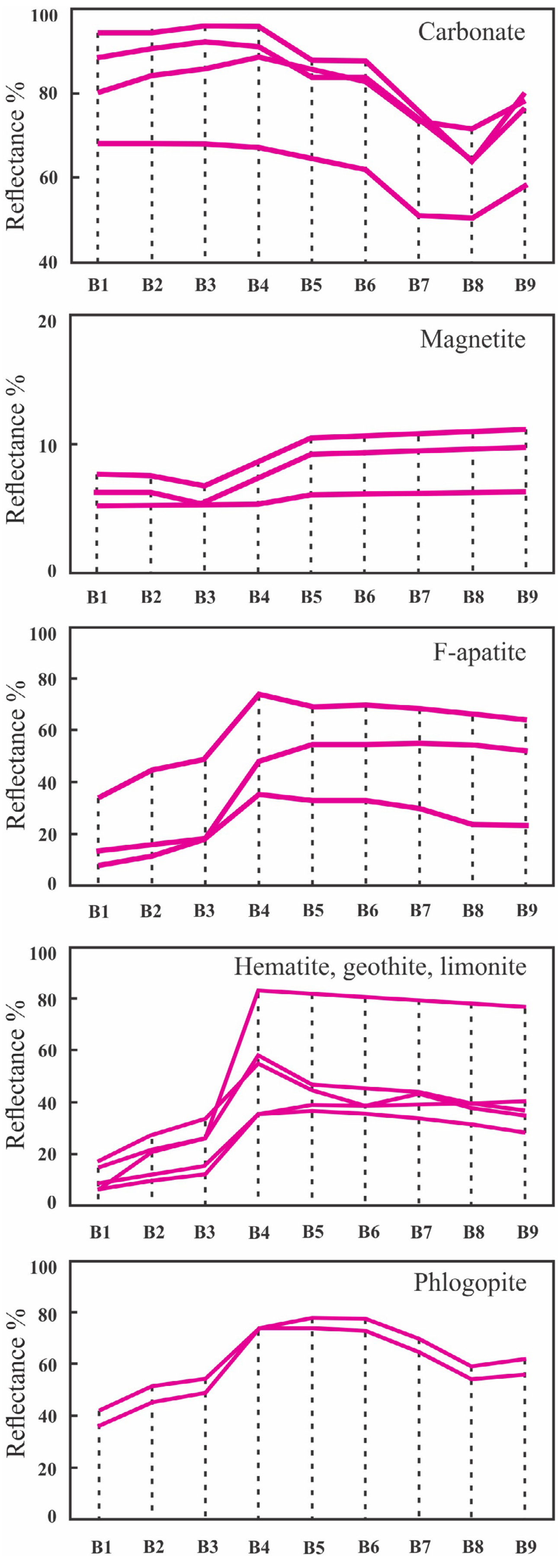

image classification (e.g., Ahmad & Quegan, 2012; Jia & Richards, 1994; Malainine et al., 2022). It is based on a discriminant function that assigns each pixel to the appropriate class based on the highest likelihood to the training areas. The accuracy of the ML classification was assessed using a confusion matrix, which is based on the comparison of the reference data and the corresponding results.

4 | RESULTS

4.1 | Mapping of carbonatite and related mineral deposits

The spectral signature of carbonate minerals show maximum absorption in bands 8 and 7 compared to neighboring bands 6 and 9 (Figure 3). Therefore, the following ASTER band ratios have been used as the most optimal choices: (B7/B8), (B6/B8), (B6/B8) * (B9/B8), (B6 + B8)/B7, (B6 + B9)/B7, and (B6/B7) * (B9/B8). Besides carbonates, it can also be perceived from Figure 3 that the most indicative minerals for carbonatite (i.e., phlogopite, apatite, and magnetite, and its alteration to hematite, goethite, and limonite) show similar absorption and reflection features, with characteristic absorption at band 3 to band 1 and high reflectance in band 4 of ASTER data. Consequently, band ratios B4/B3, and B2/B1, and B4/B1 were also used to map carbonatites and related mineral deposits of iron oxide and apatite.

Among the computed band ratios, B4/B3 has successfully mapped CRMD (Figure 4a), with the highest AUC value (0.72) compared to the other band ratios (Figure 5). Besides, (B6/B7) * (B9/B8) has a good performance with AUC = 0.64 compared to the other tested band ratios for highlighting carbonatites (Figure 4b). However, the band ratio (B6/B7) * (B9/B8) presents enhanced results due to presence of similar spectral signature of metasedimentary dolomite (carbonate rock) along the northern contact of carbonatite intrusion in the study area. Therefore, only band ratio B4/B3 has been consider to map carbonatites and associated mineral deposits of iron-oxide and apatite over the Loe-Shilman area. Figure 4 shows results of these two bands where the CRMD are highlighted in bright pixels.

FIGURE 3 The spectral features of the carbonates, Fe-oxide/hydroxides, apatite, and phlogopite as the most distinctive minerals of carbonatites. The spectral data are obtained from the USGS spectral library and resampled according to ASTER bands (e.g., Kokaly et al., 2017).

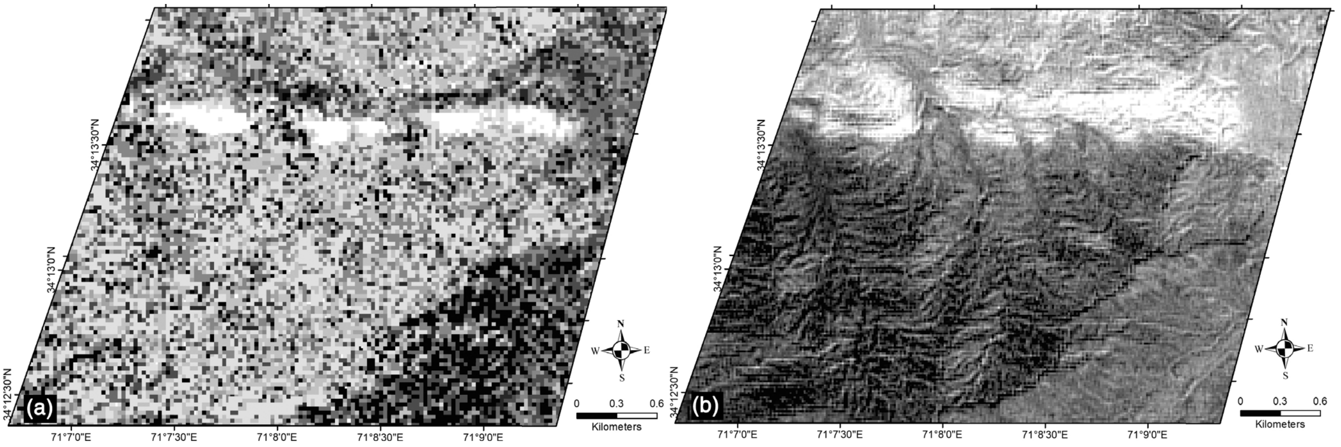

FIGURE 4 (a) Band ratio B4/B3 and (b) (B6/B7) * (B9/B8) image of the study area highlighting outcrops of the CRMD in bright pixels.

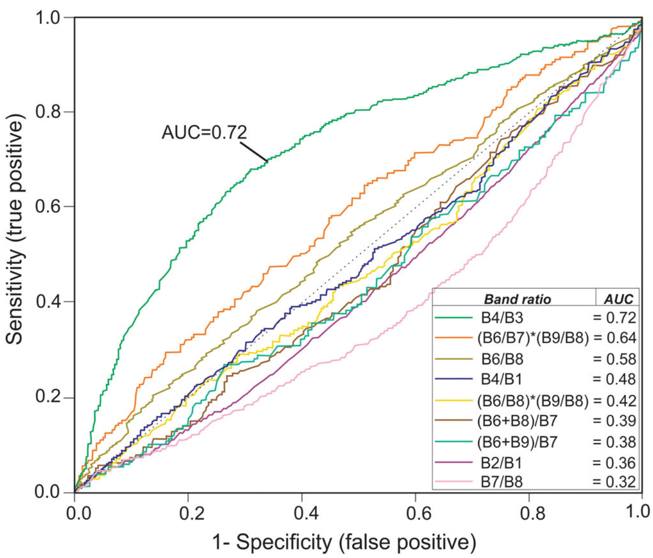

FIGURE 5 ROC curve and AUC values of carbonatites predictive band ratios.

4.2 | Principal Component Analysis

After PCA transformation the resultant eigenvectors and eigenvalues, using covariance matrix on all nine VNIR-SWIR bands of ASTER scenes covering the study area are presented in Table 3.

PC1 is composed of a positive eigenvector loading of all nine VNIR-SWIR bands. Albedo effect and scene brightness might have caused the strong correlation between multispectral image bands (e.g., Loughlin, 1991). Hence, PCA has effectively recorded albedo into PC1 of the transformed images. Eigenvector loadings for PC2 demonstrate that PC2 probably depicts the difference between the visible–near infrared channels, including bands 1, 2, and 3 (positive eigenvector loadings) and the short-wave infrared channels, including bands 4, 5, 6, 7, 8, and 9 (negative eigenvector loadings). Eigenvector loading of PC3 shows similarity with the spectral signature of Al(OH)-bearing minerals, specifically alunite and kaolinite (e.g., Mars & Rowan, 2006). These minerals have high reflectance in band 3 and 2, low reflectance in band 8 and absorptive features in bands 1, 4, 5, 6, 7, and 9, which are depicted by the eigenvector loading of PC3 (Table 3). Similarly, high eigenvector loadings in band 3 of PC4 indicate that PC4 is dominated by vegetation, because vegetation has highly reflectance in band 3 of ASTER data. Crosta et al. (1988) and Loughlin (1991) have suggested that enhancement of a mineral in PC image happens because of weighty eigenvector value for characteristic absorptive and reflective bands of mineral with opposite signs. By probing the eigenvector loadings of PC6, the high positive loadings of band 6 (0.8523) and high negative eigenvector loadings of band 8 (−0.3860) exhibit absorption and reflective features, respectively, which are similar to the spectral signatures of carbonate minerals. The negative eigenvector loading in bands 1, 2, and 3 and positive eigenvector loading in bands 4–7 in PC6 also depict the absorptive and reflective features, respectively, of other indicative minerals of carbonatites (Figure 6a). Thus, the PC6 was considered for enhancing CRMD over the Loe-Shilman area (Figure 6a). Figure 6b shows RGB false color composite of PC1, PC2, and PC6.

4.3 | Minimum Noise Fraction

The VNIR and SWIR bands of ASTER data were used as input in the MNF method and the output transformed eigenvectors are given in Table 4. The MNF5 shows a positive contributions of bands 4, 5, and 6 with negative vector loadings of bands 1, 2, 3, and 8. These

TABLE 3 Eigenvector statistics of principal components analysis on VNIR-SWIR bands of ASTER data for the study area.

Eigenvector	Band 1	Band 2	Band 3	Band 4	Band 5	Band 6	Band 7	Band 8	Band 9
PC 1	0.5587	0.4696	0.2925	0.2722	0.2580	0.2681	0.2504	0.2490	0.2109
PC 2	0.5875	0.2333	0.0969	−0.3528	−0.3081	−0.3643	−0.3254	−0.3434	−0.1230
PC 3	−0.5371	0.6596	0.3696	−0.1548	−0.2418	−0.0654	−0.0676	0.1855	−0.1186
PC 4	0.0906	0.2979	−0.7595	−0.3362	−0.0968	−0.0307	0.2243	0.3903	0.0145
PC 5	0.0137	0.1888	−0.1335	0.1393	0.3582	0.0557	0.1485	−0.2480	−0.8438
PC 6	−0.0643	−0.0019	−0.0008	0.2707	0.0606	0.8523	0.1874	−0.3860	0.0918
PC 7	0.1510	−0.3143	0.2877	−0.2035	−0.5349	0.2319	0.5275	0.1837	−0.3199
PC 8	0.1513	−0.1653	0.0129	0.2640	−0.1033	−0.0234	−0.5716	0.6570	−0.3321
PC 9	0.0124	−0.1879	0.2869	−0.6787	0.5847	−0.0801	−0.0222	0.2671	−0.0387

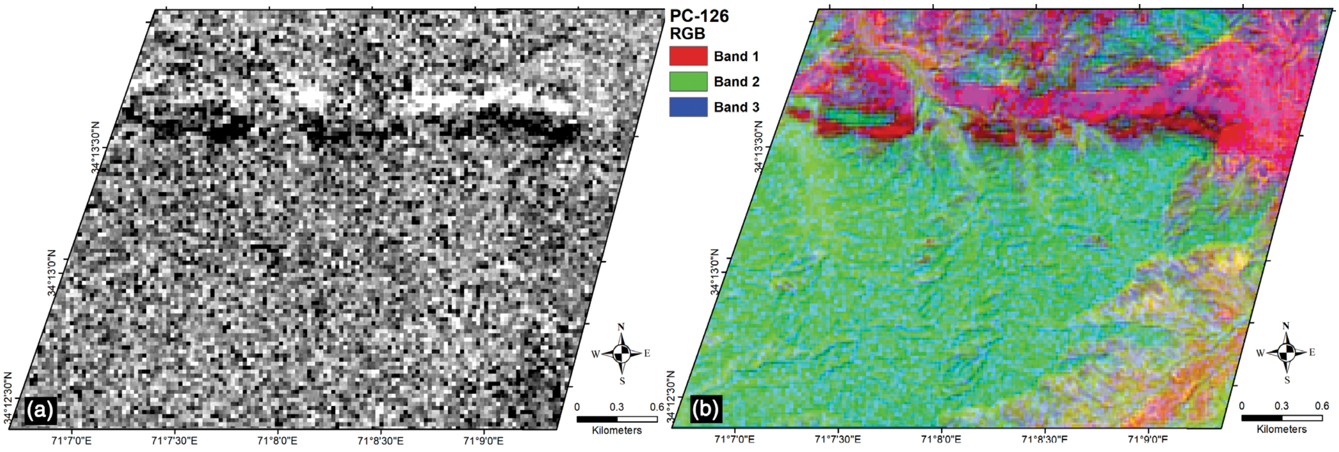

FIGURE 6 (a) PC6 transformed and (b) RGB-false color composite of PC1, PC2, and PC6 images of the study area.

TABLE 4 Eigenvector statistics of MNF transformation on VNIR-SWIR bands of ASTER data for the study area.

Eigenvector	Band 1	Band 2	Band 3	Band 4	Band 5	Band 6	Band 7	Band 8	Band 9
MNF 1	−0.9585	−0.2640	−0.0119	0.0090	0.0198	−0.0530	−0.0739	−0.0020	0.0530
MNF 2	−0.2152	0.6504	0.6089	0.1685	0.0127	0.2877	0.1376	−0.1549	−0.0750
MNF 3	−0.1258	0.2042	−0.3150	−0.2599	0.1432	0.0892	0.4106	0.3739	−0.6624
MNF 4	−0.0616	0.2266	−0.3891	0.0951	0.1541	0.3976	0.2845	0.2952	0.6591
MNF 5	−0.0244	−0.1457	−0.3204	0.3343	0.2992	0.5365	0.1690	−0.5716	0.1764
MNF 6	−0.0798	0.2646	−0.1483	0.0062	−0.7606	−0.4473	0.3251	−0.0211	0.1299
MNF 7	0.0295	−0.1417	0.1357	0.0149	0.4813	−0.4250	0.6472	−0.3304	0.1419
MNF 8	0.0864	−0.4607	0.5347	0.0367	−0.2236	0.1340	0.3140	0.5685	0.0581
MNF 9	0.0122	−0.0103	−0.1537	0.9339	0.0745	−0.1518	−0.0136	0.1687	−0.2163

characteristics are showing similarities to the spectral characteristics of most indicative minerals of carbonatite (apatite, phlogopite, hematite, limonite, and goethite), and likely the CRMD are classified in this component as dark pixels (Figure 7a). Thus, MNF4 was chosen among the other components to enhance the outcrops of CRMD in the study area. Figure 7b shows RGB false color composite of MNF1, MNF2, and MNF5.

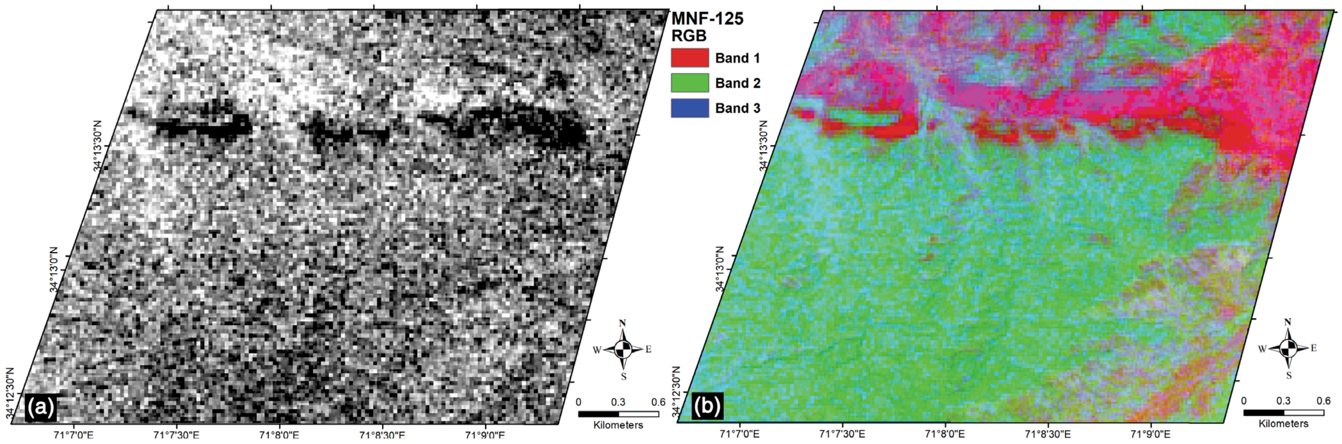

FIGURE 7 (a) MNF5 transformed and (b) RGB-false color composite of MNF1, MNF2, and MNF5 images of the study area.

4.4 | Relative accuracy assessment

The most appropriate band ratio (i.e., B4/B3) and selected components from PCA and MNF transformations (i.e., PC6 and MNF5) were reclassified and thresholded to extract the most representative pixels for CRMD in each method. It was observed that these applied methods yield different carbonatite anomalies, in some areas, which might be due to difference in sensitivities of these methods to the targeted materials occurring in the scene (Figures 4a, 6, and 7). Therefore, to check the relative accuracy of the applied methods an integrated map was produced by reclassifying the resultant images and combining all the methods (i.e., band ratio, PCA, and MNF). For this purpose, the bright pixels in band ratio image B4/B3, representing outcrops of CRMD were classified as 1 while all other pixels as 0 (Figure 8a). Similarly, the dark red pixels in RGB color composite of PC 1, 2, 6 transformed images and of MNF 1, 2, 5 (Figures 6b and 7b) were classified as 1 and all other pixels as 0 (Figure 8b,c).

After reclassification, it was found that the pixels representing CRMD in PC6 and MNF5 images occur in a relatively restricted areas, which is 15.36% and 19.35% of the total study area (Table 5). While, the band ratio B4/B3 image yield a large number of pixels representing outcrops of CRMD in the study area (i.e., 29.60% of the study area). To evaluate the success and responses of all of the methods applied and correlate their results, three different classes were generated (Table 6), which are presented in Figure 9. Class 1 represents those areas where only one method, anyone of the three methods, represents exposures of CRMD; class 2 represents areas where any two of the methods simultaneously depict outcrops of CRMD; while class 3 represents areas where all of the methods applied are showing CRMD occurrences commonly. It can be observed that there is a decrease in the number of pixels representing CRMD from class 1 to class 3. Class 1 and 2 represent 64.31% and 29.99% of the total pixels representing possible CRMD in the study area, whereas class 3 has only 5.70% pixels (Table 6).

4.5 | Field visit and absolute accuracy assessment

A field work was carried out in the Loe-Shilman area to validate the accuracy of the methods applied for mapping the occurrences of CRMD (Figure 9). Most of the areas, where the occurrences of CRMD were highlighted, were visited and several samples were collected for petrographic and chemical analyses. The carbonatites occur as white, pale brown to brown, medium- to coarse-grained rocks (Figure 10). Mineralogicaly they are dominantly composed of calcite (61%–72%), and contain variable amounts of F-apatite (10%–15%), phlogopite (10%–15%), Ca + Na- to Na-amphiboles (i.e., richterite to magnesio-arfvedsonite; 10%–15%), magnetite (3%–5%), and trace amount of pyrochlore, zircon and monazite (Figure 10). Humid-subtropical to tropical climatic conditions of the area has caused intensive weathering of the carbonatites and has developed a supergene laterite layer of variable thickness over the carbonatite complex. The supergene lateritic layer is dark brown and is consist of hematite, goethite, magnetite, limonite, zircon, pyrochlore, monazite, apatite and rutile with relicts of carbonatites. Chemically, the carbonatites are high in CaO (29.11–50.39 wt%), Fe_2O_3 (2.61–12.60 wt%), MgO (0.81–17.10 wt%) and P_2O_5 (1.29–6.48 wt%), and low in SiO_2 (2.49–7.51 wt%), Al_2O_3 (0.17–0.98 wt%), TiO_2 (0.02–0.73 wt%), MnO (0.24–1.95 wt%) and alkalis ($Na_2O + K_2O < 2$ wt%) (Khan, Faisal, Larson, et al., 2021).

During field observations it was observed that the class 3 has effectively and accurately mapped outcrops of the CRMD. It was also observed that band ratio B4/B3

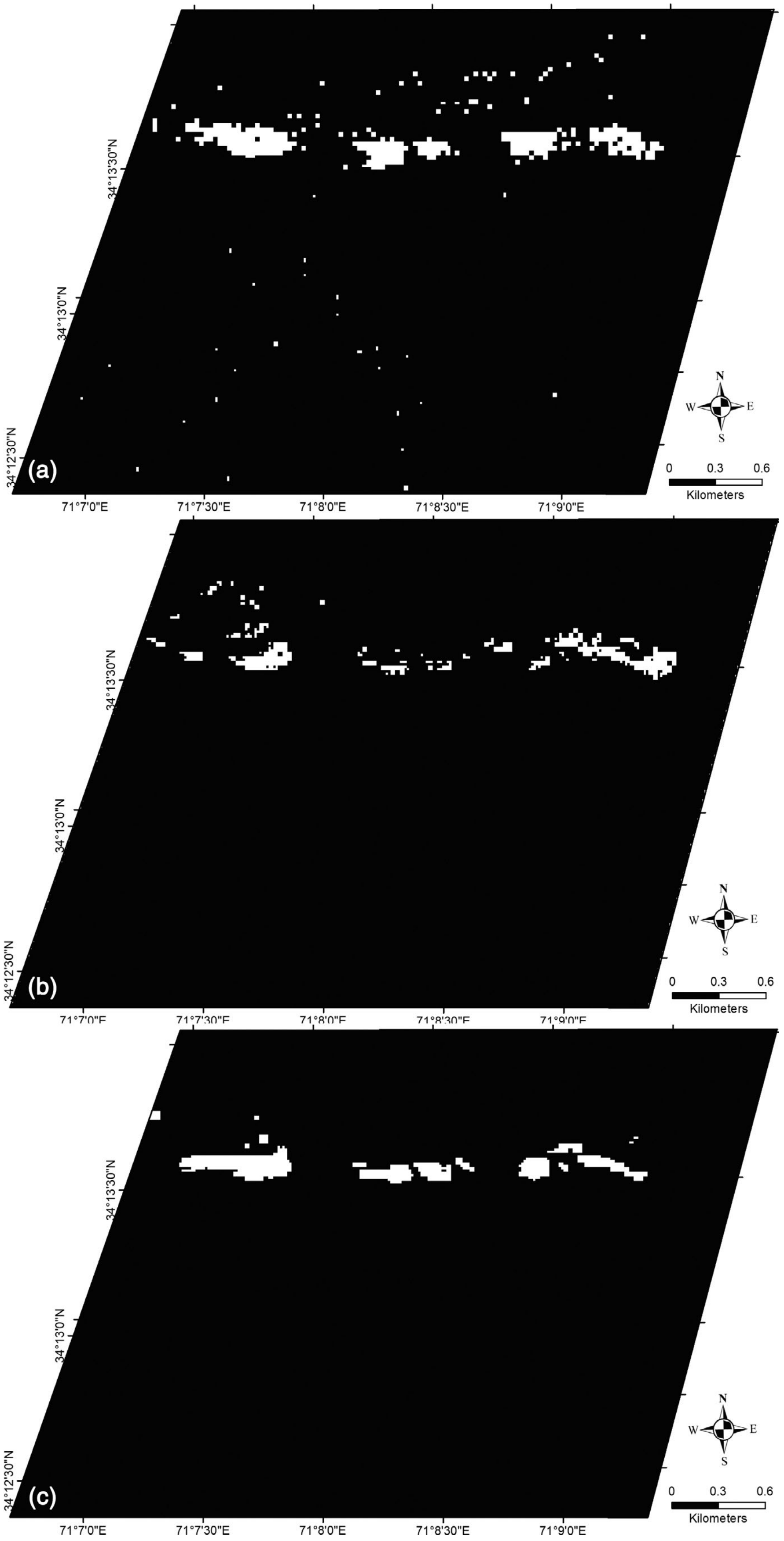

FIGURE 8 Showing reclassified images of (a) band ratios, (b) PCA, and (c) MNF. The brighter pixels are representing exposures of CRMD.

TABLE 5 Number and percentage of pixels mapped as carbonatites and related minerals by all the methods.

Method	Number of pixels	Percentage (%)	Area (m^2)
BR	1453	29.60	326,925
MNF	950	19.35	213,750
BR + MNF	642	13.08	144,450
PCA	754	15.36	169,650
PCA + BR	402	8.19	90,450
PCA + MNF	428	8.72	96,300
PCA + BR + MNF	280	5.70	63,000

TABLE 6 The three classes that were generated and their number and percentage of pixels.

Class	Number of pixels	Percentage (%)	Area (m^2)
1	3157	64.31	710,325
2	1472	29.99	331,200
3	280	5.70	63,000

has given some false results of mapping CRMD, which are scattered in the band ratio B4/B3 image (Figures 4a and 8a).

4.6 | Supervised classification-based mapping

The results obtained from the integration of the different methods were used to perform a supervised classification. As confirmed by field observations that class 3 coincides well with the outcrops of CRMD; therefore, along with other ground control points collected during the field visit, this class was used for lithological mapping of the Loe-Shilman area (Figure 11). The results were analyzed with the existing geological map of the area which show an overall accuracy of 83.01% with a kappa coefficient of 77%.

5 | DISCUSSION

Based on ASTER remote sensing and field data, an integrated approach has been tried in this study, to map outcrops of carbonatites and associate mineral deposits in Loe-Shilman area in the vicinity of Pakistan-Afghanistan boarder, in Northwest of Pakistani Himalayas. A number of band ratios have been tested to better discriminate the occurrence of CRMD from the surrounding rocks in the area. The study area also contain meta-sedimentary carbonate rocks in close contact with the carbonatites. Therefore, the previously proposed band ratios (i.e., (B6/B8) × (B9/B8) and (B6 + B8)/B7)) by Ninomiya (2002), Rowan and Mars (2003), Ninomiya et al. (2005), and Mars and Rowan (2011) for mapping carbonate minerals cannot be applied here because of similar spectral characteristics of carbonate minerals in both meta-sedimentary carbonates and carbonates of the carbonatites. Among the several other band ratio tested for mapping CRMD, band ration B4/B3 has produced better results compared to others, likely due to maximum reflective and absorption characteristics in band 4 and band 3, respectively, of distinctive non-carbonate minerals of carbonatites. However, as shown in Figure 8a, this band ration might produce some false carbonatite pixels/ areas when applied separately. These false detection of carbonatite pixels were likely due to presence of some Fe-rich rocks in the area. The PCA and MNF transformation when applied to all the nine VNIR-SWIR bands of ASTER data highlight outcrops of CRMD in PC6 and MNF5 transformed images, respectively. Eigenvector loadings of PC6 transformed image record highly positive value in band 6 (0.8523) and highly negative value in band 8 (−0.3860). Similarly, the eigenvector loadings of PC6 transformed image are negative in bands 1, 2, and 3 and positive in bands 4–7, demonstrating similarity to the spectral signatures of carbonates and other distinctive minerals of carbonatites. The eigenvector loadings of MNF5 transformed image are positive in bands 4, 5, and 6 and negative in bands 1, 2, 3, and 8, which are identical to the most indicative minerals of carbonatites (apatite, hematite, goethite, and phlogopite). While using the transformation techniques (i.e., PCA and MNF) bands 3, 4, 6, and 8 appear as the most suitable spectral bands where CRMD have diagnostic absorption and reflectance in these bands. In fact, the carbonates have significant narrow absorption in band 8 due to C—O bonds (e.g., Mars & Rowan, 2010) and high reflectance in band 6, while bands 3 and 4 have spectral characteristics for non-carbonate indicative minerals of carbonatites.

When combining band ratio with results obtained from PCA and MNF, the common pixels representing CRMD, presented better concordance with exposures of CRMD in the field. This validates the significance of

FIGURE 9 Reclassified map of CRMD exposures. Class 1 represents those areas where only one method; class 2 any two methods and class 3 all of the methods are commonly giving possible exposures of CRMD. Locations of the areas visited and samples collected for methods validation are also shown.

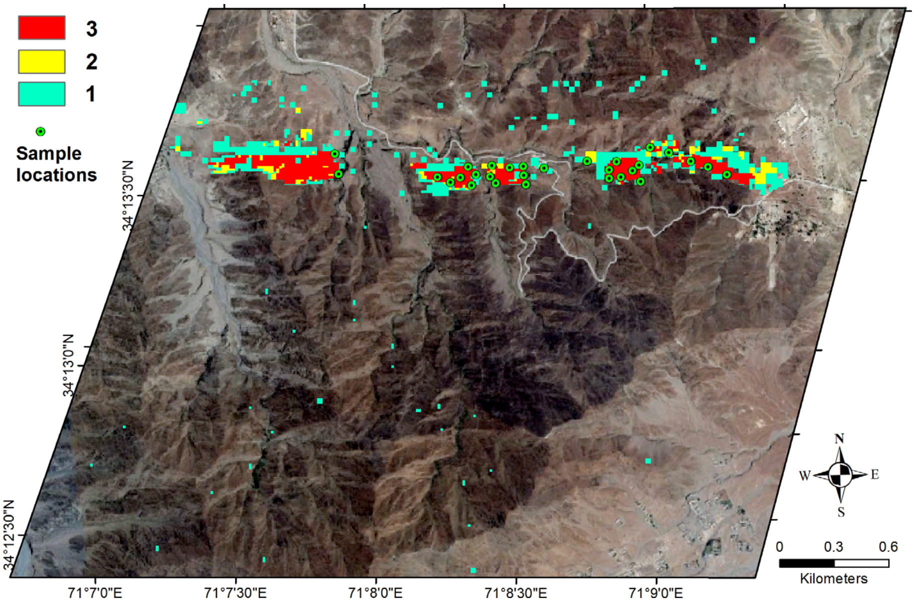

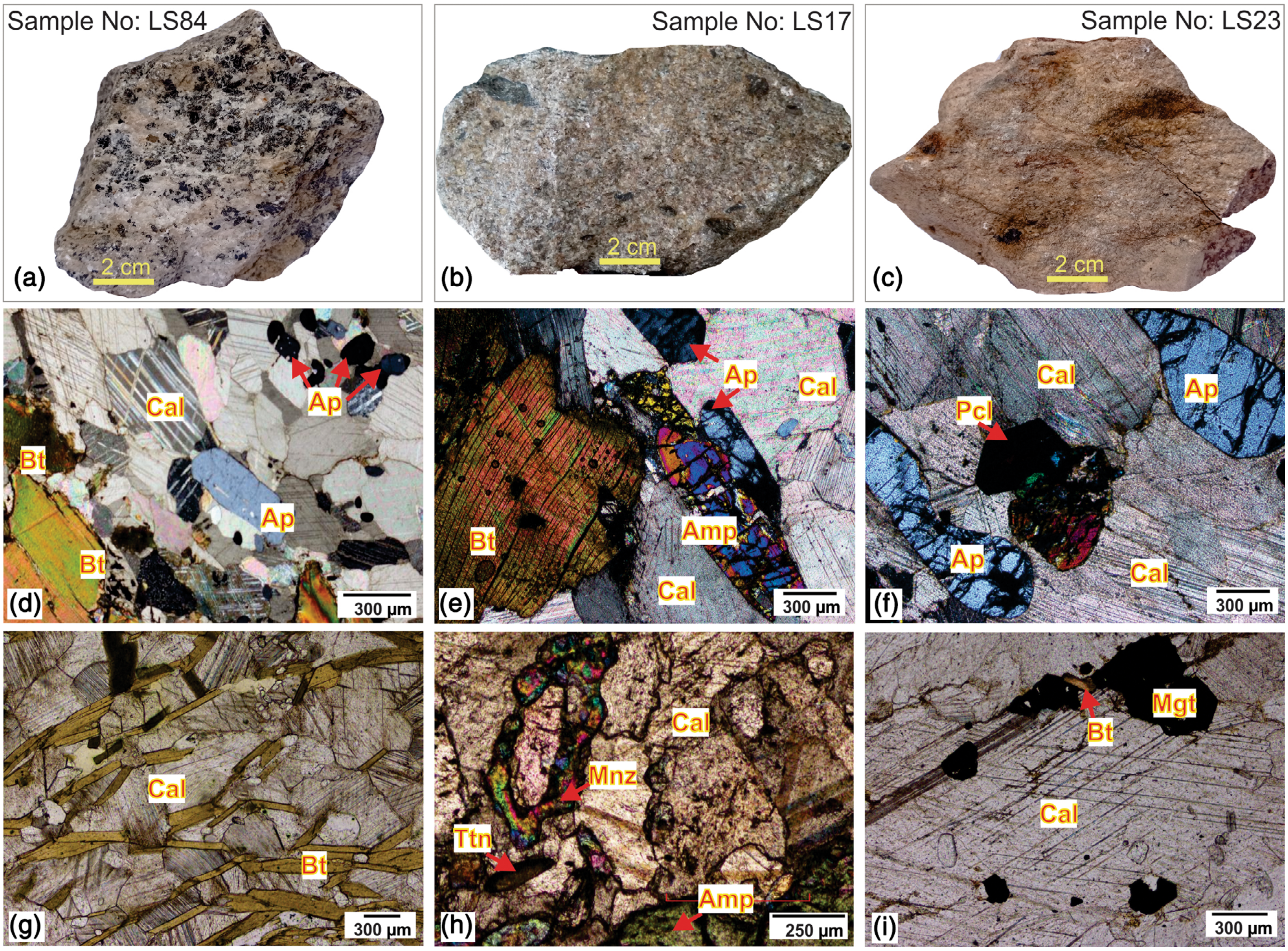

FIGURE 10 Hand specimens and photomicrographs of carbonatites showing their mineralogical compositions. (Cal: calcite); (Bt: biotite, compositionally it is phlogopite); (Ap: Apatite); (Amp: amphibole); (Pcl: pyrochlore); (Mnz: monazite); (Ttn: titanite); (Mgt: magnetite).

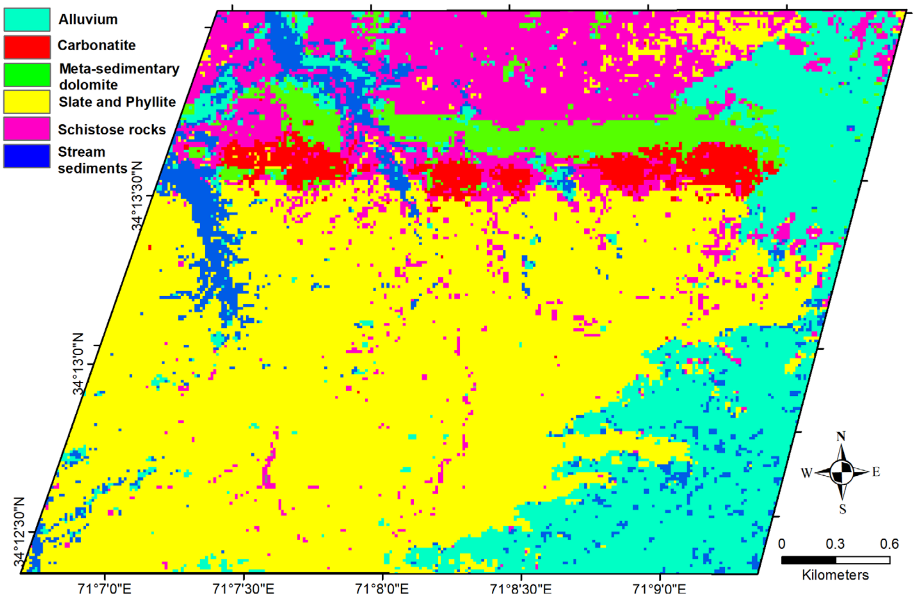

FIGURE 11 Maximum likelihood classified image of the study area.

combining the methods applied. Most of the points sampled as CRMD during the field visit fit with the common pixels for CRMD given by all of the applied methods (class 3), with few points that were only mapped by two or one methods (class 1 and class 2; Figure 8), which is likely due to different sensitivity of the applied methods.

The obtained results were validated through field surveys, chemical and petrographic analyses, which show good agreement with previous geological maps of the study area (e.g., Jan et al., 1981; Khan, Faisal, Larson, et al., 2021; Khan, Faisal, Ullah, et al., 2021). The field data were used to validate several zones mapped as possible CRMD by the different methods and validate the performed classification. The pixels classified as outcrop of CRMD by the ML-algorithm are concordant with those commonly detected by the method combinations (Figure 9). Indeed, the pixels classified as CRMD (Figure 11) show more surface extension and complete those observed in class 3 and 2 of the integrated map (Figure 9). The ML algorithm based-classification has an overall accuracy of 83% and the kappa coefficient calculated using the confusion matrix method is 0.86, which is considered as an excellent agreement category of the Kappa coefficient (e.g., Monserud & Leemans, 1992).

6 | CONCLUSIONS

This study demonstrate the suitability of ASTER data for exploration of carbonatites and related minerals in arid and inaccessible areas. Among several band ratios selected on the basis of spectral characteristics of carbonates and other distinctive minerals of carbonatites, band ratio B4/B3 has proven to give better results compared to others band ratios for enhancing outcrops of CRMD. The PCA and MNF transformation when applied to all the nine VNIR-SWIR bands of ASTER data highlight CRMD in PC6 and MNF5 transformed images, respectively. These three methods have different sensitivities for mapping CRMD; however when the pixels mapped as possible CRMD by all of the applied methods were stacked, the common pixels were a better fit with exposures of CRMD in the field. Therefore, this integrated approach may be a useful tool for exploring CRMD in other parts of the world, particularly in arid areas, and may be a time- and cost-effective tool in inaccessible remote areas where the conventional geological mapping is difficult and requires large investments.

CONFLICT OF INTEREST STATEMENT

Authors declare no conflict of interests for this article.

DATA AVAILABILITY STATEMENT

The data that support the findings of this study are available from the corresponding author upon reasonable request.

ORCID

Asad Khan https://orcid.org/0000-0002-8651-308X

REFERENCES

Abrams, M. (2000) The Advanced Spaceborne Thermal Emission and Reflection Radiometer (ASTER): data products for the high spatial resolution imager on NASA's Terra platform. *International Journal of Remote Sensing*, 21(5), 847–859.

Adler-Golden, S., Berk, A., Bernstein, L., Richtsmeier, S., Acharya, P., Matthew, M. et al. (1998) FLAASH, a MODTRAN4 atmospheric correction package for hyperspectral data retrievals and simulations. Proc. 7th Ann. *JPL Airborne Earth Science Workshop*, 97, 9–14.

Ahmad, A. & Quegan, S. (2012) Analysis of maximum likelihood classification on multispectral data. *Applied Mathematical Sciences*, 6(129), 6425–6436.

Amer, R. & Kusky, T.M. (2022) ASTER analysis for locating REE-bearing granites in arid regions: example from the Arabian shield. *Journal of Earth Science*, 33(5), 1114–1123.

Boardman, J.W., Kruse, F.A. & Green, R.O. (1995) Mapping target signatures via partial unmixing of AVIRIS data. In: *Summaries of the fifth annual JPL airborne earth science workshop. Volume 1: AVIRIS workshop*.

Burg, J.P. (2011) The Asia–Kohistan–India collision: review and discussion. In: Brown, D. & Ryan, P.D. (Eds.) *Arc-continent collision*. Berlin, Heidelberg: Springer Berlin Heidelberg, pp. 279–309.

Chakhmouradian, A.R., Reguir, E.P., Kressall, R.D., Crozier, J., Pisiak, L.K., Sidhu, R. et al. (2015) Carbonatite-hosted niobium deposit at Aley, northern British Columbia (Canada): mineralogy, geochemistry and petrogenesis. *Ore Geology Reviews*, 64, 642–666.

Clark, R.N. (1999) Spectroscopy of rocks and minerals, and principles of spectroscopy. In: Rencz, A.N. & Ryerson, R.A. (Eds.) *Remote sensing for the earth sciences: manual of remote sensing*, Vol. 3. New York: John Wiley & Sons, pp. 3–58.

Cooley, T., Anderson, G.P., Felde, G.W., Hoke, M.L., Ratkowski, A.J., Chetwynd, J.H. et al. (2002) FLAASH, a MODTRAN4-based atmospheric correction algorithm, its application and validation. *IEEE International Geoscience and Remote Sensing Symposium*, 3, 1414–1418.

Crosta, A., De Souza Filho, C., Azevedo, F. & Brodie, C. (2003) Targeting key alteration minerals in epithermal deposits in Patagonia, Argentina, using ASTER imagery and principal component analysis. *International Journal of Remote Sensing*, 24(21), 4233–4240.

Crosta, A., Moore, J. & Canasas, A. (1988) Enhancement of landsat thematic mapper imagery for mineral prospecting in weathered and vegetated terrain in SE Brazil. In: *International geoscience and remote sensing symposium, 'remote sensing: moving toward the 21st century'*, vol. 1, pp. 620.

DiPietro, J.A. & Isachsen, C.E. (2001) U-Pb zircon ages from the Indian plate in Northwest Pakistan and their significance to Himalayan and pre-Himalayan geologic history. *Tectonics*, 20(4), 510–525.

Fujisada, H. (1995) Design and performance of ASTER instrument. *Advanced and Next-Generation Satellites*, 2583, 16–25.

Green, A.A., Berman, M., Switzer, P. & Craig, M.D. (1988) A transformation for ordering multispectral data in terms of image quality with implications for noise removal. *IEEE Transactions on Geoscience and Remote Sensing*, 26(1), 65–74.

Groves, D. & Gwalani, L. (2004) Preface-special issue: carbonatites and associated mineralization. *Mineralogy and Petrology*, 80(3–4), 123–126.

Hong, J., Khan, T., Li, W., Khalil, Y.S., Narejo, A.A., Rashid, M.U. et al. (2021) SHRIMP U–Pb ages, mineralogy, and geochemistry of carbonatite–alkaline complexes of the Sillai Patti and Koga areas, NW Pakistan: implications for petrogenesis and REE mineralization. *Ore Geology Reviews*, 139, 104547.

Jagoutz, O.E., Burg, J.-P., Hussain, S., Dawood, H., Pettke, T., Iizuka, T. et al. (2009) Construction of the granitoid crust of an island arc part I: geochronological and geochemical constraints from the plutonic Kohistan (NW Pakistan). *Contributions to Mineralogy and Petrology*, 158(6), 739–755.

Jan, M.Q., Kamal, M. & Qureshi, A.A. (1981) Petrography of Shilman carbonatite complex, Khyber Agency. *Geologival Bullettin University of Peshawar*, 17, 61–68.

Jia, X. & Richards, J.A. (1994) Efficient maximum likelihood classification for imaging spectrometer data sets. *IEEE Transactions on Geoscience and Remote Sensing*, 32(2), 274–281.

Khan, A., Faisal, S., Larson, K.P., Robinson, D.M., Li, H., Ullah, Z. et al. (2023) Geochemistry and in-situ U-Th/Pb geochronology of the Jambil meta-carbonatites, northern Pakistan: implications on petrogenesis and tectonic evolution. *Journal of Earth Science*, 34(1), 70–85.

Khan, A., Faisal, S., Larson, K.P., Robinson, D.M., Ullah, Z., Li, H. et al. (2021) New geochronological and geochemical constraints on petrogenesis and tectonic setting of the Loe-Shilman carbonatite complex, Northwest Pakistan. *Lithos*, 404, 106497.

Khan, A., Faisal, S., Shafique, M., Khan, S. & Bacha, A.S. (2020) ASTER-based remote sensing investigation of gypsum in the Kohat Plateau, North Pakistan. *Carbonates and Evaporites*, 35, 1–13.

Khan, A., Faisal, S., Ullah, Z., Ali, L., Ghaffari, A., Nawab, J. et al. (2021) Pyrochlore-group minerals from the Loe-Shilman carbonatite complex, NW Pakistan: implications for evolution of carbonatite system. *Periodico di Mineralogia*, 90(2), 277–287.

Khan, S.D., Walker, D.J., Hall, S.A., Burke, K.C., Shah, M.T. & Stockli, L. (2009) Did the Kohistan-Ladakh island arc collide first with India? *Geological Society of America Bulletin*, 121(3–4), 366–384.

Kokaly, R., Clark, R., Swayze, G., Livo, K., Hoefen, T., Pearson, N. et al. (2017) *USGS spectral library version 7 data: US geological survey data release*. Reston, VA, USA: United States Geological Survey (USGS), p. 61.

Loughlin, W. (1991) Principal component analysis for alteration mapping. *Photogrammetric Engineering and Remote Sensing*, 57(9), 1163–1169.

Malainine, C.E., Raji, O., Ouabid, M., Bodinier, J.L. & El Messbahi, H. (2022) Prospectivity mapping of carbonatite-associated iron oxide deposits using an integration process of ASTER and Sentinel-2A multispectral data. *International Journal of Remote Sensing*, 43(13), 4951–4983.

Mars, J.C. & Rowan, L.C. (2006) Regional mapping of phyllic- and argillic-altered rocks in the Zagros magmatic arc, Iran, using Advanced Spaceborne Thermal Emission and Reflection Radiometer (ASTER) data and logical operator algorithms. *Geosphere*, 2(3), 161–186.

Mars, J.C. & Rowan, L.C. (2010) Spectral assessment of new ASTER SWIR surface reflectance data products for spectroscopic mapping of rocks and minerals. *Remote Sensing of Environment*, 114(9), 2011–2025.

Mars, J.C. & Rowan, L.C. (2011) ASTER spectral analysis and lithologic mapping of the Khanneshin carbonatite volcano, Afghanistan. *Geosphere*, 7(1), 276–289.

Mashkoor, R., Ahmadi, H., Rahmani, A.B. & Pekkan, E. (2022) Detecting Li-bearing pegmatites using geospatial technology:

the case of SW Konar Province, eastern Afghanistan. *Geocarto International*, 37, 1–22.

Mian, I. & Le Bas, M. (1988) Feldspar solid solution series in fenites from Loe-Shilman carbonatite complex, NW Pakistan. *Geological Bullettin University of Peshawar*, 21, 71–83.

Monserud, R.A. & Leemans, R. (1992) Comparing global vegetation maps with the Kappa statistic. *Ecological Modelling*, 62(4), 275–293.

Ninomiya, Y. (2002) Mapping quartz, carbonate minerals, and mafic-ultramafic rocks using remotely sensed multispectral thermal infrared ASTER data. *Thermosense XXIV*, 4710, 191–202.

Ninomiya, Y., Fu, B. & Cudahy, T.J. (2005) Detecting lithology with Advanced Spaceborne Thermal Emission and Reflection Radiometer (ASTER) multispectral thermal infrared "radiance-at-sensor" data. *Remote Sensing of Environment*, 99(1–2), 127–139.

Nykänen, V., Lahti, I., Niiranen, T. & Korhonen, K. (2015) Receiver operating characteristics (ROC) as validation tool for prospectivity models—a magmatic Ni–Cu case study from the Central Lapland Greenstone Belt, Northern Finland. *Ore Geology Reviews*, 71, 853–860.

Ouabid, M., Raji, O., Dautria, J.M., Bodinier, J.L., Parat, F., El Messbahi, H. et al. (2021) Petrological and geochemical constraints on the origin of apatite ores from Mesozoic alkaline intrusive complexes, Central High-Atlas, Morocco. *Ore Geology Reviews*, 136, 104250.

Öztan, S.N. & Süzen, L.M. (2011) Mapping evaporate minerals by ASTER. *International Journal of Remote Sensing*, 32(6), 1651–1673.

Pour, A.B. & Hashim, M. (2011) Identification of hydrothermal alteration minerals for exploring of porphyry copper deposit using ASTER data, SE Iran. *Journal of Asian Earth Sciences*, 42(6), 1309–1323.

Qari, M., Madani, A., Matsah, M. & Hamimi, Z. (2008) Utilization of Aster and Landsat data in geologic mapping of basement rocks of Arafat Area, Saudi Arabia. *The Arabian Journal for Science and Engineering*, 33(1C), 99–116.

Rajendran, S. & Nasir, S. (2013) ASTER spectral analysis of ultramafic lamprophyres (carbonatites and aillikites) within the Batain Nappe, northeastern margin of Oman: a proposal developed for spectral absorption. *International Journal of Remote Sensing*, 34(8), 2763–2795.

Rajendran, S. & Nasir, S. (2014) ASTER spectral sensitivity of carbonate rocks—study in Sultanate of Oman. *Advances in Space Research*, 53(4), 656–673.

Raji, O., Ouabid, M., Bodinier, J.-L., El Messbahi, H., Malainine, C.E. & Tabbakh, Z. (2021) An integrated approach for rapid delineation of K-rich syenites suitable as unconventional potash resources. *Natural Resources Research*, 30(5), 3219–3239.

Rehman, H.U., Seno, T., Yamamoto, H. & Khan, T. (2011) Timing of collision of the Kohistan–Ladakh Arc with India and Asia: debate. *Island Arc*, 20(3), 308–328.

Rowan, L.C. & Mars, J.C. (2003) Lithologic mapping in the Mountain Pass, California area using advanced spaceborne thermal emission and reflection radiometer (ASTER) data. *Remote Sensing of Environment*, 84(3), 350–366.

Sabins, F.F. (1999) Remote sensing for mineral exploration. *Ore Geology Reviews*, 14(3–4), 157–183.

Searle, M. & Treloar, P. (2010) Was Late Cretaceous–Paleocene obduction of ophiolite complexes the primary cause of crustal thickening and regional metamorphism in the Pakistan Himalaya? *Geological Society, London Special Publications*, 338(1), 345–359.

Singh, A. & Harrison, A. (1985) Standardized principal components. *International Journal of Remote Sensing*, 6(6), 883–896.

Son, Y.S., Lee, G., Lee, B.H., Kim, N., Koh, S.M., Kim, K.E. et al. (2022) Application of ASTER data for differentiating carbonate minerals and evaluating MgO content of magnesite in the Jiao-Liao-Ji Belt, North China craton. *Remote Sensing*, 14(1), 181.

Su, J.H., Zhao, X.F., Li, X.C., Hu, W., Chen, M. & Xiong, Y.L. (2019) Geological and geochemical characteristics of the Miaoya syenite-carbonatite complex, Central China: implications for the origin of REE-Nb-enriched carbonatite. *Ore Geology Reviews*, 113, 103101.

Tobin, D.C., Antonelli, P.B., Revercomb, H.E., Dutcher, S.T., Turner, D.D., Taylor, J.K. et al. (2007) Hyperspectral data noise characterization using principle component analysis: application to the atmospheric infrared sounder. *Journal of Applied Remote Sensing*, 1(1), 013515.

Toledo, M.C.M.D., Lenharo, S.L., Ferrari, V.C., Fontan, F., De Parseval, P. & Leroy, G. (2004) The compositional evolution of apatite in the weathering profile of the Catalão I alkaline-carbonatitic complex, Goiás, Brazil. *The Canadian Mineralogist*, 42(4), 1139–1158.

Traore, M., Can, T. & Tekin, S. (2022) Mapping carbonate-hosted Pb-Zn mineralization zones in Yahyali Province (Eastern Taurus-Turkey) using ASTER data. *Advances in Space Research*, 69(1), 266–281.

Yamaguchi, Y., Fujisada, H., Kudoh, M., Kawakami, T., Tsu, H., Kahle, A. et al. (1999) ASTER instrument characterization and operation scenario. *Advances in Space Research*, 23(8), 1415–1424.

Zaitsev, A.N., Williams, C.T., Jeffries, T.E., Strekopytov, S., Moutte, J., Ivashchenkova, O.V. et al. (2015) Rare earth elements in phoscorites and carbonatites of the Devonian Kola Alkaline Province, Russia: examples from Kovdor, Khibina, Vuoriyarvi and Turiy Mys complexes. *Ore Geology Reviews*, 64, 477–498.

How to cite this article: Khan, A., Ali, M., Khan, S., Ullah, Z., Faisal, S. & Ahmad, L. (2023) An integrated approach for rapid exploration of carbonatites and related mineral resources. *Resource Geology*, 73(1), e12321. Available from: https://doi.org/10.1111/rge.12321